Impacts of the Phase Shift between Incident Radar Waves on the Polarization Variables from Ice Cloud Particles

VALERY MELNIKOV

Cooperative Institute for Mesoscale Meteorological Studies, University of Oklahoma, and NOAA/OAR/National Severe Storms Laboratory, Norman, Oklahoma

(Manuscript received 29 November 2019, in final form 4 June 2020)

ABSTRACT

The impacts of the differential phase of incident radar waves (ψ_i) on measured differential reflectivity (Z_{DR}), differential phase, and correlation coefficient from ice cloud particles are presented for radars employing simultaneous transmission and reception of orthogonally polarized waves (SHV radar design). The maximal values of Z_{DR} and the differential phase upon scattering (δ) from ice particles are obtained as functions of ψ_i. It is shown that SHV δ from ice particles can exceed a dozen degrees whereas the intrinsic δ is of a few hundredths of a degree. In melting layers, the δ values from particles obeying the Rayleigh scattering law can be several degrees depending on ψ_i so that, to explain such δ values, an assumption of resonance scattering is not necessary. The phase δ affects the estimation of specific differential phase (K_{DP}) in icy media and, therefore, the phase δ should be measured. The radar differential phase upon transmission ψ_t is a part of ψ_i and, therefore, affects the δ values. A radar capability to alter ψ_i by varying ψ_t could deliver additional information about scattering media.

1. Introduction

Radar precipitation measurements and target recognitions are based on the intrinsic reflectivity, differential reflectivity (Z_{DR}), differential phase (Φ_{DP}), and copolar correlation coefficient (ρ_{hv}). The intrinsic radar variables are measured with radars employing the alternate transmission of horizontally and vertically polarized waves (AHV radar design; e.g., Bringi and Chandrasekar 2001, sections 4.1.1 and 4.1.2). However, the vast majority of polarimetric weather radars transmit horizontally and vertically polarized waves simultaneously (SHV radar design). The SHV design is technically simpler than the AHV one (Doviak at al. 2000; Bringi and Chandrasekar 2001). On the other hand, the SHV variables are biased because the main backscattered waves interact with the depolarized waves. The differential phase ψ_i between the waves incident on scatterers plays a crucial role in this interaction. The general consensus is that the SHV polarimetric variables are sufficiently close to the AHV ones in measurements in rain (Doviak et al. 2000; Wang et al. 2006). In measurements in ice media, the difference between the SHV and AHV radar variables can be large (e.g., Doviak et al. 2000, section 6; Ryzhkov and Zrnić 2007; Hubbert et al. 2014a,b). The difference between the variables from AHV and SHV radars have been considered using intrinsic Z_{DR}, ρ_{hv}, and the linear depolarization ratio (Doviak at al. 2000; Wang et al. 2006; Bringi and Chandrasekar 2001, section 4.7), which are not measured with SHV radars. A different approach is utilized in this study: the impacts of ψ_i are obtained by using physical parameters of scatterers known from the literature.

Impacts of ψ_i on the SHV variables from icy areas of thunderstorms, where ice particles can be aligned by in-cloud electric fields, are considered in sections 2 and 3. The SHV variables for ice ellipsoids, hexagonal prisms, and dendrites are analyzed. Stratiform clouds do not typically have strong electric fields. In such clouds, ice particles flutter in the air and fall with their longest axes oriented horizontally in the mean (Pruppacher and Klett 1997, section 10.5). Impacts of ψ_i on radar variables from fluttering ice particles are presented in section 4.

A focus of this study is the differential phase ψ_i consisting of two addends:

Supplemental information related to this paper is available at the Journals Online website: https://doi.org/10.1175/JTECH-D-19-0197.s1.

Corresponding author: Valery Melnikov, valery.melnikov@noaa.gov

DOI: 10.1175/JTECH-D-19-0197.1

$$\psi_{\mathrm{i}} = \psi_{\mathrm{t}} + \varphi_{\mathrm{dp}}, \tag{1}$$

where ψ_{t} is the phase shift between horizontally and vertically polarized waves upon transmission and φ_{dp} is the one-way propagation differential phase. The φ_{dp} value is used in calculations of the specific differential phase (K_{DP}). In snow and ice clouds, K_{DP} at S band are of a fraction of a degree per kilometer that requires precise measurements of the total differential phase Φ_{DP}, which depends on correct estimation of the phase upon scattering (δ). The intrinsic δ for ice particles at centimeter wavelengths is of a few hundredths of a degree whereas the SHV δ values depend on ψ_{i} and can be of several degrees (section 4) and, therefore, the differential phase ψ_{i} plays an important role in K_{DP} estimations. Impacts of ψ_{i} on δ, Φ_{DP}, and K_{DP} in ice media should be thoroughly studied. Some aspects of these impacts are presented here.

The following questions are addressed in this study using known microphysical properties of ice particles:

- What is the maximal Z_{DR} and δ from ice particles observed with SHV radar? How does ψ_{i} affect these maximal values? How does ψ_{i} impact Z_{DR} and δ from ice particles of different habits (section 2)?
- The phase δ from stratiform clouds can be linked to microphysical properties of scatterers. How does ψ_{i} affect measured δ (section 4)?
- Measurements of δ values in melting layers show some increase compared to values above the layers. This increase is explained with possible presence of large wet particles of resonance sizes (e.g., Trömel et al. 2013, 2014). Is it possible to explain such δ values by scattering from Rayleigh ice particles (section 5)?

Another motivation for studying impacts of ψ_{i} on SHV variables is the possibility of obtaining additional information about scatterers. According to (1), ψ_{i} can be changed by varying the phase ψ_{t}. In a conventional SHV radar, the phase ψ_{t} can be altered with phase shifters, which are mechanical devices featuring long switching times as compared to typical radar dwell times. A phased array radar is capable of changing ψ_{t} during the dwell time by varying the time delay between the transmitted waves that could be used for obtaining additional information about scatterers in real time.

2. Maximal Z_{DR} and δ from ice particles as functions of ψ_{i}

Positive and negative Z_{DR} and K_{DP} are frequently observed in thunderstorms, where strong in-cloud electric fields orient ice particles along the fields. Cloud areas with aligned particles can be observed with radars (e.g., Hendry and McCormick 1976; Caylor and Chandrasekar 1996). SHV radars detect particles having common vertical tilts of their major axes. Vertically aligned ice particles produce negative Z_{DR} and K_{DP}. In some cases, fields of Z_{DR} and Φ_{DP} exhibit stripe patterns (e.g., Ryzhkov and Zrnić 2007; Hubbert et al. 2018). Maximal values of Z_{DR} and δ from ice particles are of interest.

Ice cloud crystals in forms of plates and columns frequently have shapes of hexagonal prisms (Fig. 1). Scattering properties of such particles can be obtained with the discrete dipole approximations (Purcell and Pennypacker 1973; Draine and Flatau 1994), scattering models based on the methods of moments (e.g., WIPL-D 2020; FEKO 2020; Chobanyan et al. 2015), and the finite element method (e.g., ANSYS 2020) to name a few. Thin ice particles can be satisfactorily approximated with spheroids or ellipsoids that are characterized with the axis ratio of width/length = b/a (Fig. 1; e.g., Bringi and Chandrasekar 2001; Hogan et al. 2012; Matrosov 2015). The shapes of particles' edges are not important for thin particles with $a/b > 20$. Scattering properties of ellipsoids can be derived analytically in the Rayleigh limit (e.g., Bohren and Huffman 1983, section 5.3) or obtained numerically at any size/wavelength ratio (e.g., Mishchenko et al. 2002) that makes ellipsoids convenient model scatterers. Scattering geometry can be described using the scattering plane (e.g., Holt 1984; Vivekanandan et al. 1991; Ryzhkov and Zrnić 2007); here, the laboratory frame affixed to the ground is used (frame OXYZ in Fig. 1). This frame naturally describes orientations of cloud particles relative to the ground and to a radar beam. In this frame, θ is the canting angle of a particle and the incident waves are horizontally and vertically polarized at low antenna elevation angles.

The Z_{DR} and δ values from pristine cloud particles depend on their shape, axis ratio, dielectric permittivity, and orientation relative to the polarization planes of incident waves. In thunderstorms, ice particles can be aligned at any θ and φ by in-cloud electric fields and, therefore, these angles can lie in intervals $0° \le \theta \le 180°$ and $0° \le \varphi \le 360°$.

Scattering of horizontally (subscript h) and vertically (subscript v) polarized electromagnetic waves by a single scatterer is described by the scattering matrix $\mathbf{S}$ with the elements S_{mn} (m and n are any of h and v). Let E_{hi} and E_{vi} be the amplitudes of the incident waves (Fig. 1); then the scattered (subscript s) waves E_{hs} and E_{vs} are written as

$$\begin{pmatrix} E_{\mathrm{hs}} \\ E_{\mathrm{vs}} \end{pmatrix} = \begin{pmatrix} S_{\mathrm{hh}} & S_{\mathrm{hv}} \\ S_{\mathrm{hv}} & S_{\mathrm{vv}} \end{pmatrix} \begin{pmatrix} E_{\mathrm{hi}} \\ E_{\mathrm{vi}} e^{j\psi_{\mathrm{i}}} \end{pmatrix}, \tag{2}$$

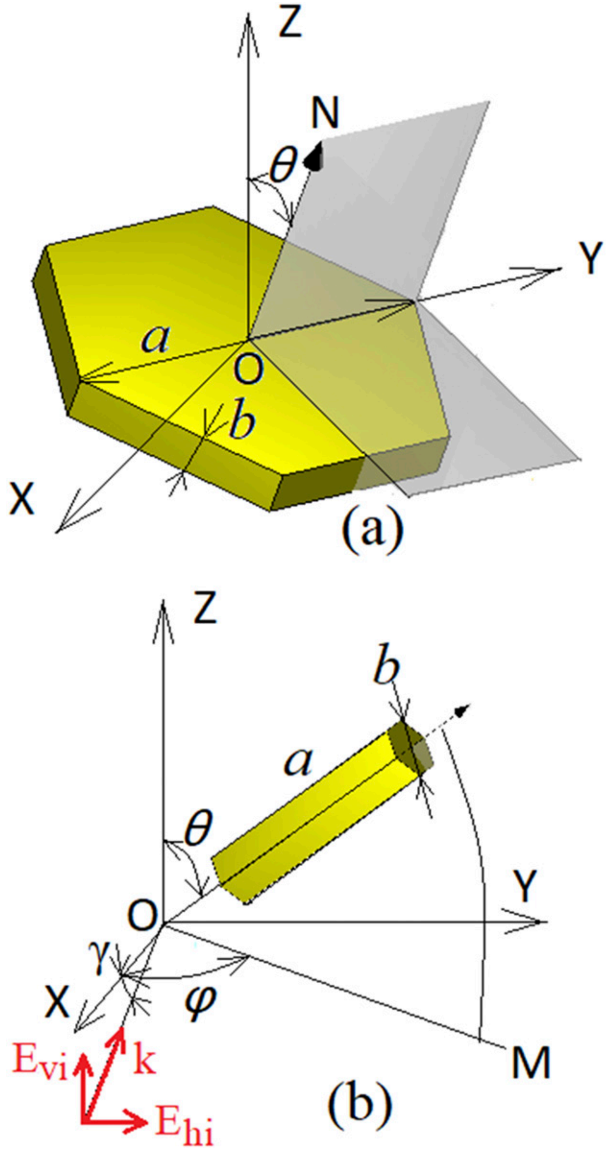

FIG. 1. Geometry of scattering by (a) platelike and (b) columnar hexagonal ice particles. E_{hi} and E_{vi} are the amplitudes of incident horizontally and vertically polarized waves propagating in direction **k**. The plane OXY is horizontal and ON is orthogonal to the plate's face. The angles θ and γ are the canting and antenna elevation angles, respectively. OM is horizontal, **k** lies on the plane OXZ, and φ is orientation angle of the particle's axis.

where ψ_{i} is the differential phase between the incident waves and j is imaginary unity. The latter equation is written in the backscatter alignment; therefore, $S_{\mathrm{hv}} = S_{\mathrm{vh}}$. The differential phase ψ_{i} in (2) signifies that the incident vertically polarized wave is ahead of the horizontally polarized wave by ψ_{i}.

SHV radar typically transmits waves of different amplitudes and phases because the signal paths and amplifications in the radar channels are different. Gains in the received polarization channels may also be different. Corrections for the system amplitude imbalances are done in Z_{DR} calibration, but the transmitted and received waves remain shifted in phase. The one-way propagation phase adds to the phase shifts between the incident waves [see (1)]. After Z_{DR} calibration, the transmitted wave amplitudes can be considered equal; i.e., $E_{\mathrm{vi}} = E_{\mathrm{hi}} = E$ at negligible differential attenuation. The scattered waves acquire δ at scattering and the propagation differential phase φ_{dp} on their way back to the radar. The received waves also get shifted by ψ_{r} by the radar chains so that the total phase shift at a radar signal processor is $\psi_{\mathrm{r}} + \psi_{\mathrm{i}} + \varphi_{\mathrm{dp}} + \delta$. The received waves from a single scatterer can be written as

$$\begin{pmatrix} E_{\mathrm{hr}} \\ E_{\mathrm{vr}} \end{pmatrix} = C_R \begin{pmatrix} 1 & 0 \\ 0 & e^{j(\psi_{\mathrm{r}}+\varphi_{\mathrm{dp}})} \end{pmatrix} \begin{pmatrix} S_{\mathrm{hh}} & S_{\mathrm{hv}} \\ S_{\mathrm{hv}} & S_{\mathrm{vv}} \end{pmatrix} \begin{pmatrix} 1 & 0 \\ 0 & e^{j\psi_{\mathrm{i}}} \end{pmatrix} \begin{pmatrix} E \\ E \end{pmatrix}, \tag{3}$$

where C_R is the radar constant with the range dependence included. Note that δ does not appear in (3) explicitly and originates from the scattering matrix **S**. The first and third matrixes on the right-hand side in (3) describe propagation of the waves from radar to the resolution volume and back. The zero off-diagonal terms in the propagation matrixes signify negligible depolarization in the propagation medium in which differential attenuation is also negligible. The radar constant C_R and the amplitude E will be omitted in the following discussion because Z_{DR}, ρ_{hv}, and δ are relative values and do not depend on those; therefore,

$$E_{\mathrm{hr}} = S_{\mathrm{hh}} + S_{\mathrm{hv}} e^{j\psi_{\mathrm{i}}} \quad \text{and} \quad E_{\mathrm{vr}} = (S_{\mathrm{vv}} e^{j\psi_{\mathrm{i}}} + S_{\mathrm{hv}}) e^{j(\psi_{\mathrm{r}}+\varphi_{\mathrm{dp}})}. \tag{4}$$

The scattering matrix elements can be represented as

$$S_{\mathrm{hh}} = \alpha_a + \Delta\alpha \sin^2\theta \sin^2\varphi, \qquad S_{\mathrm{vv}} = \alpha_a + \Delta\alpha \cos^2\theta,$$
$$S_{\mathrm{hv}} = \Delta\alpha \sin\theta \cos\theta \sin\varphi, \quad \text{with} \quad \Delta\alpha = \alpha_b - \alpha_a, \tag{5}$$

where α_a and α_b are polarizabilities along the major particle's axes (α_a refers to the longer axis), [e.g., Bringi and Chandrasekar 2001, their Eq. (2.53)]. Note that the antenna angle γ is absent in (5); i.e., $\gamma = 0$ is set. For nonzero γ, (5) can be considered relative to the angle γ that will not change the maximal values in question. Substitution of (5) into (4) yields

$$E_{\mathrm{hr}} = \alpha_a + \Delta\alpha A \sin\theta \sin\varphi, \tag{6}$$

$$E_{\mathrm{vr}} = (\alpha_a e^{j\psi_{\mathrm{i}}} + \Delta\alpha A \cos\theta) e^{j(\psi_{\mathrm{r}}+\varphi_{\mathrm{dp}})}, \tag{7}$$

with $A = \sin\theta \sin\varphi + \cos\theta e^{j\psi_{\mathrm{i}}}$.

Also, Z_{DR} and δ from a single scatterer (or a collection of scatterers equally oriented) are

$$Z_{DR} = 10\log(|E_{hr}|^2/|E_{vr}|^2) \quad \text{and} \tag{8}$$

$$\delta = \arg(E^*_{hr}E_{vr}) - \psi_t - \psi_r - 2\varphi_{dp}, \tag{9}$$

where the asterisk (*) stands for complex conjugate and $E^*_{hr}E_{vr} = R_{hv}$ is the correlation function. The first addend on the right-hand side of (9) is the total measured differential phase Φ_{DP}. To obtain δ, one has to subtract the propagation and system differential phases from the measured phase. One can see from (6)–(9) that measured Z_{DR} and δ depend on ψ_i.

To make (9) clearer, consider scattering by a sphere for which $\alpha_b = \alpha_a$ and, therefore, $S_{hv} = 0$. Then $E_{hr} = \alpha_a$, $E_{vr} = \alpha_a e^{j(\psi_i+\psi_r+\varphi_{dp})}$, and $R_{hv} = |\alpha_a|^2 e^{j(\psi_i+\psi_r+\varphi_{dp})}$, the argument of which is $\psi_t + \psi_r + 2\varphi_{dp}$. According to (9), $\delta = 0$ as it should be for a sphere. So SHV δ emerges at scattering by nonspherical particles and depends on ψ_i. To calculate δ from model particles, one can set $\psi_r = \varphi_{dp} = 0$ and δ is obtained as the argument of the correlation function R_{hv} with ψ_i as an argument.

It is seen from (4) that the scattered waves have two contributions: the primary ones containing S_{hh} and S_{vv} and depolarized ones depending on S_{hv}. These mixed contributions are sometimes referred to as wave coupling upon scattering. Due to the coupling, Z_{DR} and δ values measured with SHV radar can significantly deviate from those measured with AHV radar. For AHV radar, (2) can also be used by setting $S_{hv} = 0$ and $\psi_t = 0$. For such radar, the amplitudes of received waves are $E^{AHV}_{hr} = S_{hh}$ and $E^{AHV}_{vr} = S_{vv}$; i.e.,

$$E^{AHV}_{hr} = \alpha_a + \Delta\alpha \sin^2\theta \sin^2\varphi \qquad \text{and}$$
$$E^{AHV}_{vr} = \alpha_a + \Delta\alpha \cos^2\theta. \tag{10}$$

For plates, $\Delta\alpha < 0$ and the maximal Z^{AHV}_{DR} and δ^{AHV} are attained at $\theta = 0$, i.e., at horizontal orientation of the scatterer:

$$Z^{AHV}_{DR\max} = 10\log(|\alpha_a|^2/|\alpha_b|^2) \quad \text{and} \quad \delta^{AHV}_{\max} = \arg(\alpha^*_a\alpha_b). \tag{11}$$

For a columnar scatterer, the maximal Z^{AHV}_{DR} and δ^{AHV} are attained at $\theta = \varphi = 90°$, i.e., at its horizontal orientation (Fig. 1b). For scatterers that are much smaller than the radar wavelength, i.e., in the Rayleigh scattering limit, and approximated with a spheroid, polarizabilities $\alpha_{a,b}$ are (e.g., Doviak and Zrnić 2006, section 8.5.2.4)

$$\alpha_{a,b} = V\frac{\varepsilon - 1}{1 + L_{a,b}(\varepsilon - 1)}, \tag{12}$$

where V is the scatterer's volume, ε is dielectric permittivity of ice ($\varepsilon = 3.17 - 0.0015j$ at S frequency band), and $L_{a,b}$ are the shape factors. For a very thin plate, $L_a = 0$ and $L_b = 1$, so (Vivekanandan et al. 1994; Hogan et al. 2002)

$$Z^{AHV}_{DR\max} = 20\log(|\varepsilon|) = 10\,\text{dB}. \tag{13}$$

This value varies insignificantly at centimeter wavelengths. For thin needles, $L_a = 0$ and $L_b = 0.5$; therefore,

$$Z^{AHV}_{DR\max} = 20\log(|\varepsilon + 1|/2) = 6.4\,\text{dB}. \tag{14}$$

To obtain maximal Z_{DR} for thin needles randomly oriented on the horizontal plane, one has to average $|E^{AHV}_{hr}|^2$ and $|E^{AHV}_{vr}|^2$ from (10) over the angle φ at $\theta = 90°$. The imaginary part of ε is very small compared to its real part and can be neglected, so (Hogan et al. 2002)

$$Z^{AHV}_{DR\max} = 10\log\{1 + [(|\varepsilon| - 1)/2] + [3(|\varepsilon| - 1)^2/32]\}$$
$$= 4.0\,\text{dB}. \tag{15}$$

The phase $\delta^{AHV}_{\max}$ is calculated from (11). For ice plates, $\delta^{AHV}_{\max} = -\arg(\varepsilon) = 0.03°$ and for needles, $\delta^{AHV}_{\max} = -\arg(\varepsilon + 1) = 0.02°$, i.e., very small values. Thus, the differential phase upon backscattering by ice particles is of a few hundredths of a degree for AHV radar in the Rayleigh limit. Pristine ice cloud particles are better represented with hexagonal prisms (Westbrook 2014). Values of $\alpha_{a,b}$ for very thin prisms and ellipsoids are equal so that $Z^{AHV}_{DR\max}$ and $\delta^{AHV}_{\max}$ for these shapes are also equal.

Now consider Z_{DR} and δ measured with SHV radar. Figure 2 presents Z_{DR} and δ as functions of θ(0°–180°) and φ(0°–360°) at $\psi_i = 90°$ for thin ice plates and needles. The values $\theta_{\max}$ and $\varphi_{\max}$ are angles at which Z_{DR} and δ attain their maximums. These variables for other ψ_i are shown in the online supplemental material (Fig. S1). The maximal Z_{DR} depends on ψ_i. A value of Z_{DR} =12.3 dB, the absolute maximum (maximum maximorum) for ice plates, is attained at $\psi_i = 0$, $\theta = 16°$, and $\varphi = 90°$ (or $\psi_i = 180°$, $\theta = 106°$, and $\varphi = 270°$, Fig. S1a). A tilt in the canting angle θ increases Z_{DR} over 10 dB obtained for AHV radar. For ice needles, the absolute maximum of 6.9 dB is attained at $\theta = 10°$ or 170°, $\varphi = 90°$, and $\psi_i = 0°$ (Fig. S1d).

The phase δ exhibits a strong dependence on ψ_i. At $\psi_i = 0°$, δ is very small for all θ and φ. The absolute maximum of $\delta_{\max} = 62.3°$ for plates is attained at $\theta = 50°$, $\varphi = 90°$, and $\psi_i = 60°$. For ice needles, the absolute maximum of $\delta_{\max} = 40.9°$ is attained at $\theta = 50°$, $\varphi = 90°$, and $\psi_i = 70°$. These results for maximal Z_{DR} and δ illustrate strong impacts of depolarized waves on the

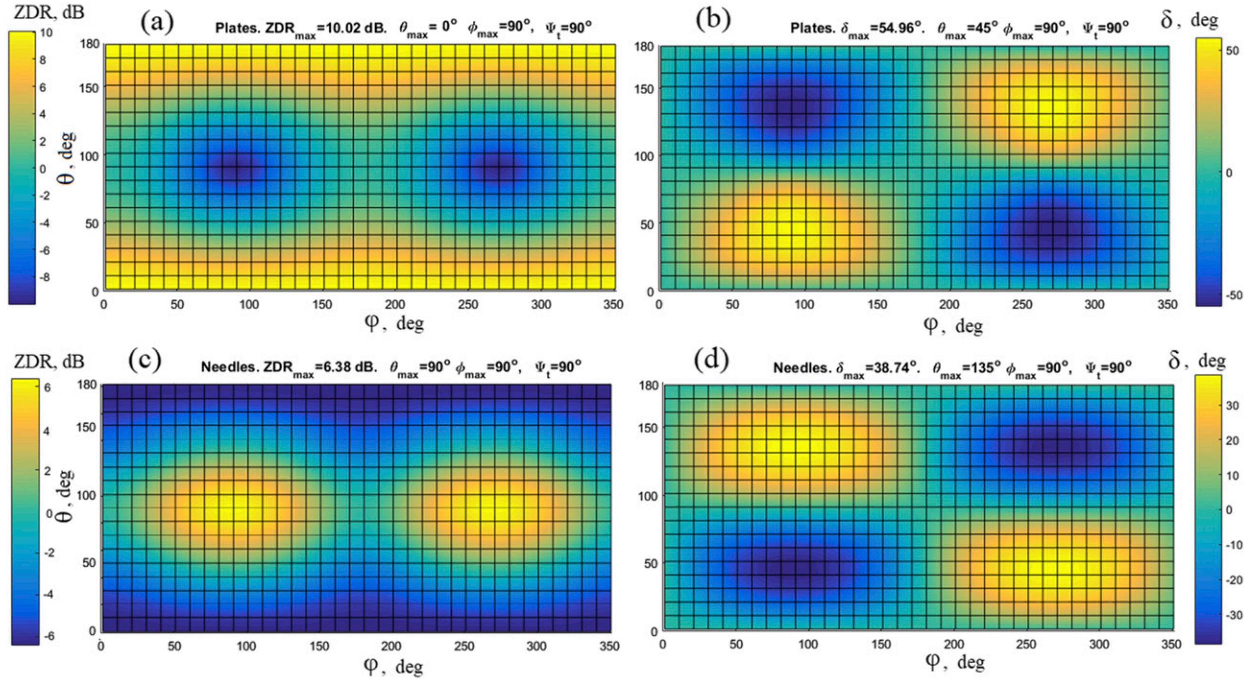

FIG. 2. (a) Z_{DR} for thin ice plates as a function of the angles θ and φ at $\psi_{\mathrm{i}} = 90°$, (b) As in (a), but for the phase δ. (c),(d) As in (a) and (b), but for ice needles.

SHV radar variables and that the wave coupling depends on ψ_{i}.

It is easy to intuitively accept that horizontally oriented particles produce positive Z_{DR} and δ and vertically oriented particles produce negative Z_{DR} and δ; i.e., these variables should be of the same sign. Figure 2 shows that the opposite situations can occur. For nearly horizontal particles, for instance, at an area about $\theta = 10°$ and $\varphi = 270°$ for plates (Fig. 2a), the Z_{DR} values are positive, but the δ values are negative (Fig. 2b; see also Fig. S2 showing radar observations). Positive δ values can be produced at negative Z_{DR}, for instance, at $\theta = 70°$ and $\varphi = 90°$ for plates (Figs. 2a,b). To reveal the source of these counterintuitive situations, examine the waves scattered by an ice plate oriented at $\theta = 10°$ and $\varphi = 270°$ at $\psi_{\mathrm{i}} = 90°$. For short, in this paragraph, H and V stand for horizontal and vertical polarizations, respectively. Obtain the contribution to the scattered waves in terms of the main H backscattered wave; i.e., let $\alpha_a = 1$. The imaginary parts of $\alpha_{a,b}$ can be neglected for ice. Then the contribution to the H wave from depolarization [see (4)] is $0.00 + 0.12j$ and the sum of the primary and depolarized waves is $1.00 + 0.12j$. The latter shows that the depolarized wave substantially increases the imaginary part of the scattered wave. Recall that the imaginary parts of waves are responsible for phase shifts; the small imaginary parts of scattered AHV waves lead to the small δ discussed above. The main V backscattered wave is $0.00 + 0.34j$; i.e., the differential phase in incident radiation contributes to a strong imaginary part of the main backscattered wave. The contribution to V wave from depolarization is $0.12 + 0j$ and their sum is $0.12 + 0.34j$. From the two amplitudes $1.00 + 0.12j$ and $0.12 + 0.34j$, the argument of correlation function is 64°. Since $\psi_{\mathrm{i}} = 90°$, the phase upon scattering is $\delta = 64° - 90° = -26°$, i.e., a large negative number. The negative phase δ is caused by strong depolarization and the incident differential phase plays a critical role in the origin of δ. For a smaller ψ_{i}, for instance, $\psi_{\mathrm{i}} = 40°$, $\delta = -14°$; i.e., δ remains negative and large. Negative δ values of $-6°$ to $-8°$ have been observed in smoke plumes containing fluttering scatterers oriented horizontally in the mean (Melnikov et al. 2008, 2009). Note that the situation of positive Z_{DR} and negative δ has its mirror counterpart; i.e., negative Z_{DR} can exhibit positive δ.

The values of $\delta_{\max}$ are large for thin ice particles (Fig. 2) and can be positive and negative depending on ψ_{i} and orientation of the scatterers. This contrasts with very small δ values at alternate polarizations. The differential phase ψ_{i} depends on the radar phase shift in transmit ψ_{t} [see (1)], so to interpret the differential phases measured with a SHV radar, ψ_{t} should be known.

The measurable SHV differential phase Φ_{DP} is

$$\Phi_{\mathrm{DP}} = 2\varphi_{\mathrm{dp}} + \psi_{\mathrm{t}} + \psi_{\mathrm{r}} + \delta. \tag{16}$$

The sum $\psi_t + \psi_r$ is called the radar system differential phase ψ_{sys}. This phase can be measured at the closest-to-radar edge of precipitation, where φ_{dp} is negligible and, therefore, $\Phi_{DP} = \psi_{sys} + \delta$. For light rain at S band $\delta \approx 0$ because the droplets are almost spherical; therefore, $\psi_{sys} = \Phi_{DP}$. Because δ can reach larger values in ice clouds, measurements of ψ_{sys} could be incorrect. The SHV δ depends on ψ_t, yet only the sum $\psi_t + \psi_r$ can be readily obtained. Separate measurements of ψ_t and ψ_r are challenging on such systems.

The positive absolute maximum Z_{DR} values as a function of ψ_i (Fig. 3a) have been obtained as maximum maximorum values on surfaces as those in Fig. 2. Positive and negative Z_{DR} and δ values are connected as $Z_{DR}(\psi_i) = -Z_{DR}(180° - \psi_i)$ and $\delta(\psi_i) = -\delta(180° - \psi_i)$.

Hexagonal prisms are a better representation of the pristine ice plates and columns than spheroids. The previous results are valid for very thin spheroids and hexagonal prisms, i.e., at $a/b \gg 1$. The maximal Z_{DR} and δ for a moderate a/b exhibit dependence on the particle's shape. The Z_{DRmax} values for spheroids are about 1 dB larger than those for prisms at a moderate axis ratio of $b/a = 0.3$ (Fig. 4a). The δ_{max} values are noticeably different for prisms and spheroids (Fig. 4b). The polarization properties of hexagonal prisms have been obtained with the NOAA release of WIPL-D package.

Dendrites and stellars are frequent habits of ice particles. The dendrite branches can have various shapes and mass. Auer and Veal (1970) documented relations between the length and width of natural dendrites. Z_{DR} and δ as functions of θ and φ for the dendrite of these dimensions (Figs. 5b,c) are close in shape to those for plates (Fig. 2 and Fig. S1), but the maximal Z_{DR} value is 4.1 dB and the maximal δ is 25.5°. Dendrites of the same lengths and width can have more subbranches and, therefore, more mass. For such dendrites, Z_{DR} and δ increase, but cannot exceed the values for the thin ice plates obtained above. It is quite obvious that, in the Rayleigh limit, an ice particle of any shape cannot produce Z_{DR} and δ values larger than those obtained for thin ice plates at the same ψ_i.

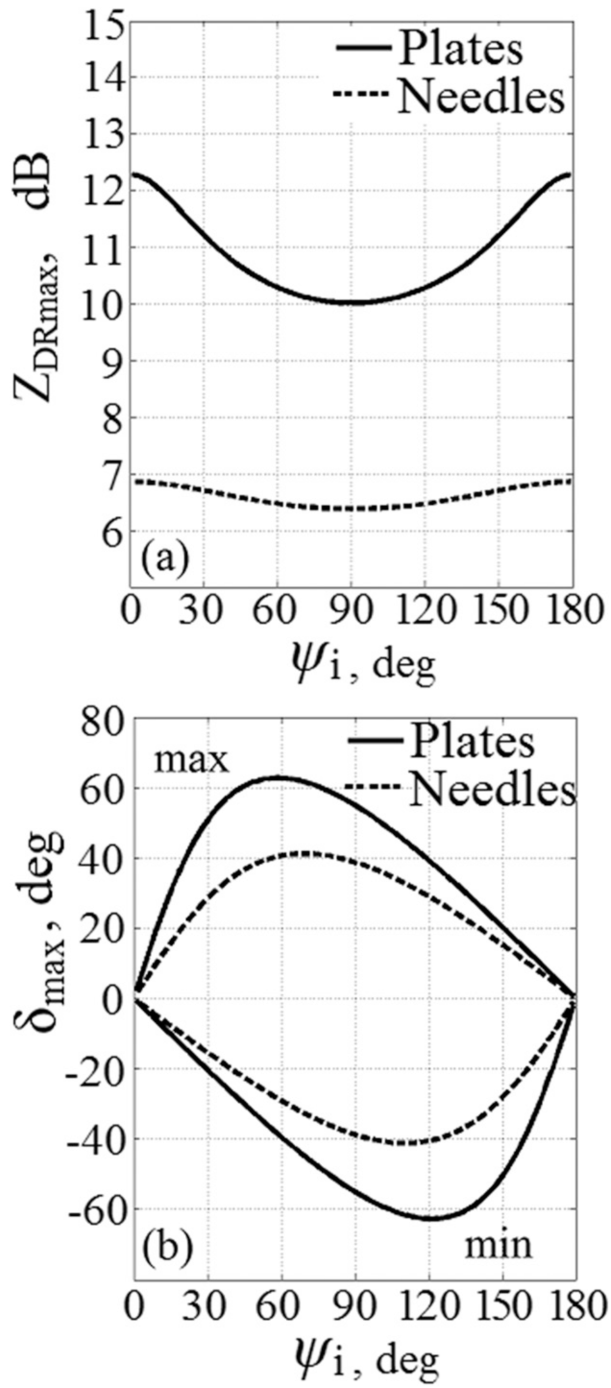

FIG. 3. (a) Z_{DRmax} and (b) δ_{max} as functions of the incident differential phase for thin ice plates (solid curves) and ice needles (dash curves).

3. An example of δ in a thunderstorm

Positive and negative SHV δ values are frequently observed in thunderstorms. The case in Fig. 6 was observed with S-band SHV WSR-88D KOUN radar located at Norman, Oklahoma [the radar parameters can be found in Doviak and Zrnić (2006), their Tables 3.1 and 6.1]. It can be seen as an increase in Φ_{DP} values at the cloud top (left panel) at heights of 12–15 km. A range profile of Φ_{DP} through this area (Fig. 7a) shows a gradual increase to a distance of 46 km and a strong bump at distances of 46–49 km. If the gradual increase is attributed to the propagation effect, then the sharp increase of about 5° should be due to δ. Similar Φ_{DP} peaks are also observed at the adjacent radials that indicates that the peak is not caused by signal fluctuations.

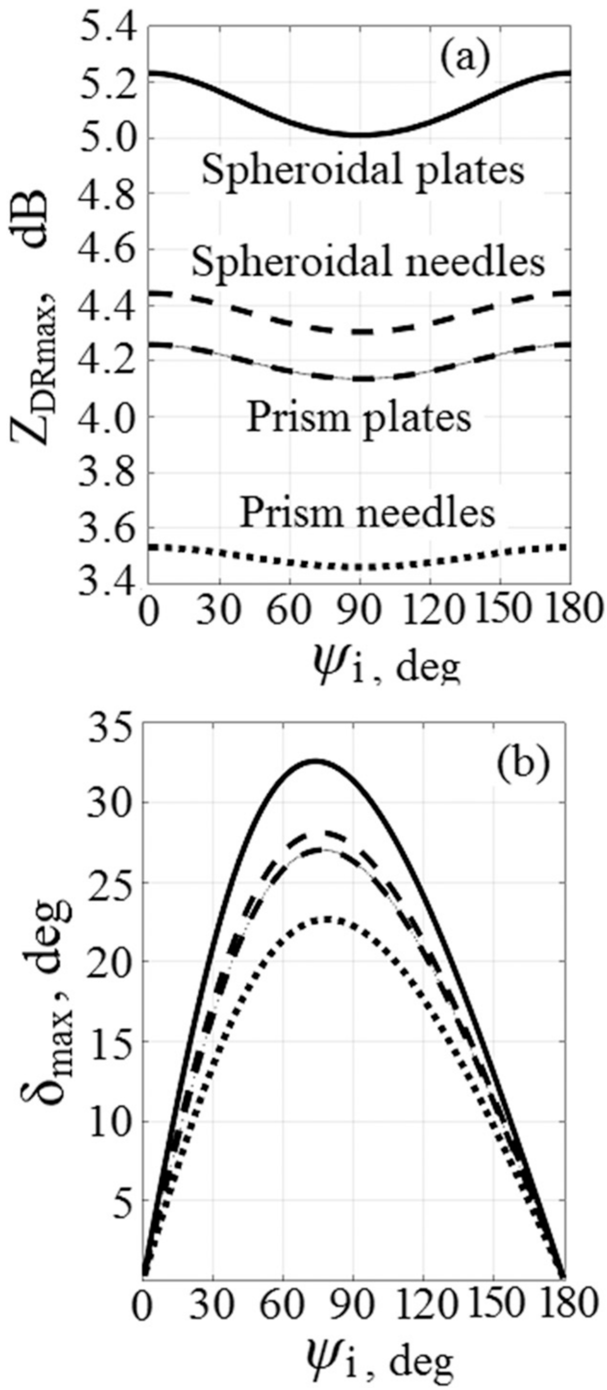

FIG. 4. As in Fig. 3, but for $b/a = 0.3$ and for spheroids and prisms. The curve labels in (a) is applicable for curves in (b).

A large area of negative Z_{DR} is seen at heights of 9–14 km, where Φ_{DP} drops by about 16° when compared to the values at the edge of the area closer to the radar. The negative Z_{DR} values indicate the presence of ice particles oriented primarily vertically. A Φ_{DP} range profile through this area (Fig. 7c) exhibits a drop of about 7° at distances from 35 to 47 km. This drop can be attributed to propagation of the waves in areas with vertically oriented particles. Between distances of 47 and 67 km, Φ_{DP} increases at negative Z_{DR} that could be due to positive δ as it was discussed in the previous section. Therefore, it is possible that positive δ values contribute to the increase in Φ_{DP} of about 16° from a range of 47 km to the end of the radial. KOUN's unknown ψ_t does not allow for a more certain interpretation. A case in Fig. S2, where a decrease in Φ_{DP} in the cloud top occurs at positive $Z_{DR,}$ is another example of difficulties in interpretations of Φ_{DP} and δ without knowing ψ_i. To narrow down uncertainties in the interpretation of Φ_{DP}, variations in ψ_i could be helpful. Such variations can be accomplished by varying ψ_t. This radar capability could deliver additional information about scattering media.

4. Impacts of ψ_i on δ and ρ_{hv} from ice stratiform clouds

Stratiform ice clouds typically do not have strong electric fields capable of aligning ice particles; therefore, ice particles fall with their major axes being horizontal in the mean (e.g., Pruppacher and Klett 1997, section 10.5). In such clouds, δ values typically vary spatially (more often in height) by about 2°–3°. For instance, compare the Φ_{DP} values at the top and bottom of a cloud in Fig. 8 at horizontal distances beyond 20 km. The median Φ_{DP} values are 3.1° and 5.4° at heights of 3–4 and 4–5 km, respectively. The propagation contribution to Φ_{DP} is negligible at S band at these distances in such clouds and, therefore, the variation in Φ_{DP} are caused by δ. Thus, the increase in δ from the top to bottom is 2.3° in the mean.

Ice particles flutter in the air. Fluttering particles produce lower Z_{DR} and ρ_{hv}. The dependences of δ values upon the flutter intensity are more complicated because the δ values are also affected by ψ_i. The δ values typically increase with the flutter intensity to some intermediate value and then decrease at stronger flutter. This initial increase is caused by the increase in δ at some nonzero canting angles (section 2). When flutter changes the canting angles close to the one that produces enhanced δ, observed δ values are larger than those for horizontal particles.

The phase δ from fluttering particles is obtained from the correlation function R_{hv} (Melnikov 2017):

$$R_{hv} = e^{j(\psi_t+\psi_r+2\varphi_{dp})}[\langle|\alpha_a|^2\rangle + \mathrm{Re}(\langle\alpha_a^*\Delta\alpha\rangle)C_4 + j\mathrm{Im}(\langle\alpha_a^*\Delta\alpha\rangle)C_5 + (\langle|\Delta\alpha|^2\rangle)C_6], \quad (17)$$

where the angle brackets stand for the size averaging and C_4, C_5, and C_6 are functions of ψ_i and the standard

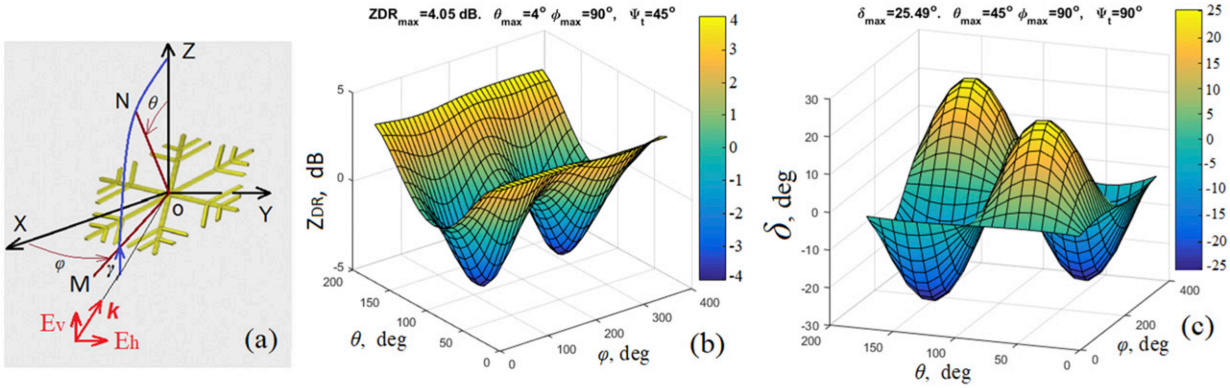

FIG. 5. (a) As in Fig. 1, but for the dendrite. (b) Z_{DR} as a function of θ and φ for the dendrite and at $\psi_i = 45°$. (c) As in (b), but for δ at $\psi_i = 90°$.

deviation σ_θ in canting angles of the particles. Alternations in the canting angles can be caused by flutter or/and asymmetry in the particles' shapes. Asymmetrical ice particles have nonzero mean canting angles and are frequently observed in clouds (e.g., Pruppacher and Klett 1997, section 2.2; Wolde and Vali 2001; Hogan et al. 2012).

Figure 9 presents ρ_{hv} and δ values for Rayleigh ice plates fluttering in the air. The standard deviation in the canting angles is 15°, which is the value obtained by Garrett et al. (2015) and Melnikov and Straka (2013). Figures 9a and 9b present results for a very thin ice plates. At $\psi_t = 0°$, the δ values are very small. The maximal δ of 7° is attained at $\psi_i = 90°$ at horizontal incidence. Note also that δ is not equal to 0° at vertical incidence for nonzero ψ_i. Nonzero ψ_i makes scattering geometry asymmetrical even though particles viewed from bottom are symmetrical. For an ice plate having the axis ratio of 0.3 (Figs. 9c,d), the ρ_{hv} values are much higher than those for the very thin plates and the δ values drop to about 2°. Note that such δ values have been observed in the case in Fig. 8.

The following conclusions can be drawn from the presented results. 1) Values of δ can be used as a property parameter of ice particles because δ depends on their axis ratio. 2) To use δ values quantitatively, the differential phase ψ_i should be measured. Since ψ_t is a part of ψ_i, the system phase upon transmission must be known (measured). 3) The phase δ should be accounted for in obtaining K_{DP} in icy media because K_{DP} is obtained from Φ_{DP}, which depends on δ [see (16)]. 4) The phase δ depends on the properties of a particle and on ψ_i (and, correspondingly, on ψ_t); therefore, additional information about particles could be obtained by varying ψ_t.

5. Impacts of ψ_i on radar variables from melting layers

Values of radar variables in melting layers (ML) frequently are quite different from those measured in areas located above and below MLs. The supplemental material contains radar images illustrating some typical situations described here. Small Z_{DR} values above the

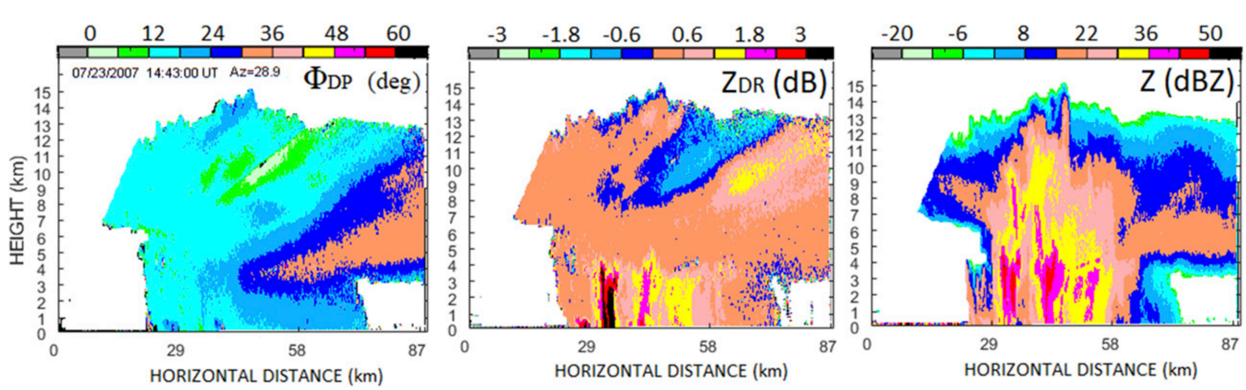

FIG. 6. Vertical cross section of a thunderstorm observed with the KOUN radar at 1443 UTC 23 Jul 2007 at an azimuth of 28.9°.

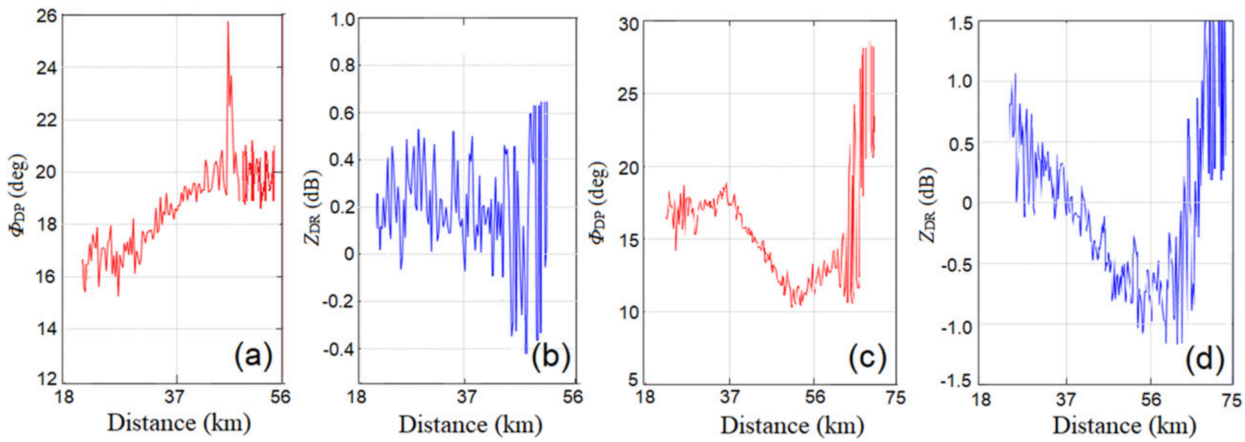

FIG. 7. (a),(b) Range profiles of Φ_{DP} and Z_{DR}, respectively, from the fields in Fig. 6 at an antenna elevation of 17.4°. (c),(d) As in (a) and (b), but for an antenna elevation angle of 11.3°.

ML can be accompanied by greater Z_{DR} values below the ML (e.g., Fig. S4) and vice versa (Figs. S5 and S7). Sometimes, a layer of low Z_{DR} values is observed just above MLs (Fig. S6) that is explained by the aggregation processes there (e.g., Griffin et al. 2020). In some situations, a layer of reduced Z_{DR} above MLs is not observed (Figs. S4, S5, and S7). Vertical stripes of enhanced Z_{DR} can be observed above MLs (Fig. S8) that could point to the presence of strong ice generating cells at the cloud tops. The Z_{DR} values inside the shown MLs span an interval from about 0.5 dB (Fig. S4) to about 5 dB (Fig. S9). Values of Z_{DR} in MLs should be analyzed at distances close to the radar because data at longer distances are smeared by increased beam broadening in range (e.g., Figs. S5 and S6 beyond a distance of 100 km).

The Φ_{DP} patterns above and below MLs can be about the same (Figs. S7 and S8), but can be quite different (Figs. S5, S6, S9, and S10). The Φ_{DP} patterns above and below MLs can have similar (Figs. S7 and S8) or quite different characteristics (Figs. S5, S6, S9, and S10). Because of short signal paths in clouds at distances shorter than 15 km, the increase in Φ_{DP} above the ML in Figs. S5 and S10, can be largely attributed to greater δ values. Significant propagation Φ_{DP} contributions are observed in icy parts of clouds in Figs. S5 and S6 whereas those contributions are very small below the MLs. In contrast, no difference in the Φ_{DP} range dependences are seen in Figs. S7 and S8. The Φ_{DP} values inside MLs typically exhibit some enhancements compared to values outside MLs. The mean enhancements typically are 2°–5° (e.g., Figs. S5 and S7), which can be largely attributed to increase in δ. Griffin et al. (2020) report on an increase in δ up to 10° in MLs. Such δ values are sometimes explained with the presence of large particles of resonance sizes (e.g., Trömel et al. 2014). It is shown in this section that the observed δ can be produced by Rayleigh particles if the incident waves are shifted in phase.

The ρ_{hv} values in MLs lie in a wide interval. In the supplemental materials, one can see ρ_{hv} values from 0.7 (Fig. S9) to 0.93 (Fig. S7) inside MLs. In areas above MLs, correlation is typically observed between ρ_{hv} and Z_{DR} values: Z_{DR} exhibit lower ρ_{hv} and vice versa (Griffin et al. 2018). Such a correspondence is evident in Fig. S5, although almost no difference in ρ_{hv} can also be observed (Fig. S6).

The described features can be observed simultaneously in various parts of a weather system (e.g., Fig. S11). Strong influence of the δ phase on the Φ_{DP} field is evident in Fig. S11: note significant variations in

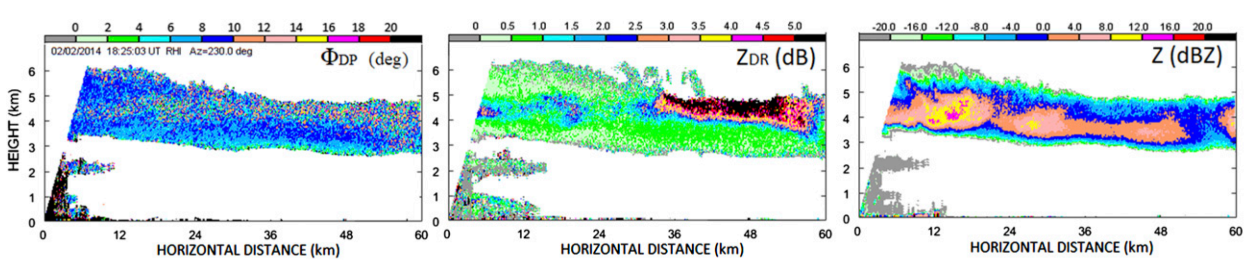

FIG. 8. As in Fig. 6, but the data were collected at 1825 UTC 2 Feb 2014 at an azimuth of 230°.

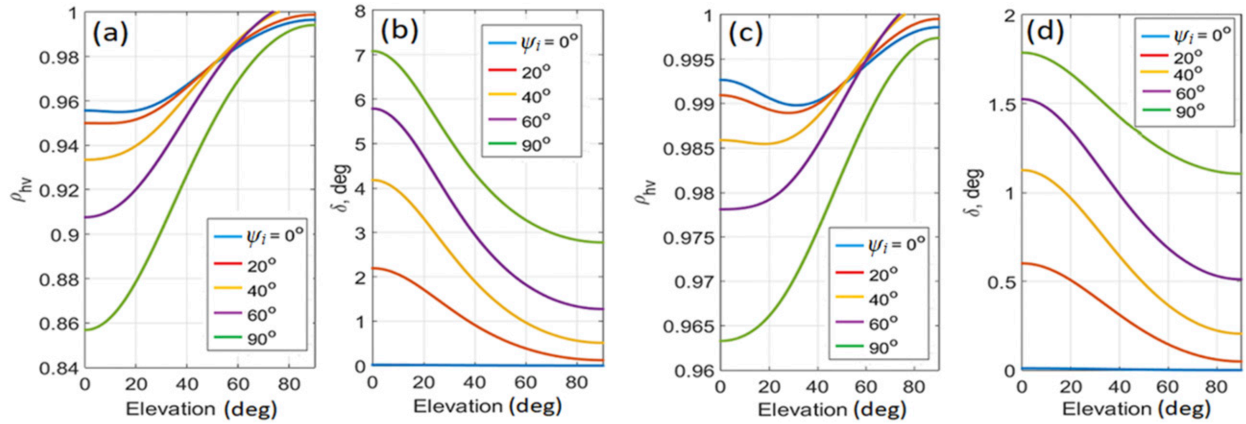

FIG. 9. (a),(b) Values of ρ_{hv} and δ, respectively, for very thin ice plates as functions of the antenna elevation angle and indicated differential phase ψ_i. The standard deviation in the canting angles is 15°. (c),(d) As in (a) and (b), but for an axis ratio $b/a = 0.3$.

Φ_{DP} at distances within 30 km and above the ML, the decreases in Φ_{DP} at ranges 40–50 and 60–80 km in rain areas and at ranges about 60–70 and 130–140 km in the cloud tops.

This short review of the radar variables measured inside and above MLs point to a variety of shapes of particles falling into MLs and various compositions of ice and water in particles inside MLs. Water in ice particles can be a result of their melting and can also be acquired at a collision of an ice particle with water droplets emerged from already melted particles. To study the impacts of the differential phase ψ_i on the radar variable from MLs, simple models of wet ice particles have been analyzed and the results follow.

If no aggregation above an ML takes place, an ice particle inside an ML retains the shape it had above the ML and can get coated with a thin water film in the ML. Let ice particles be approximated with oblate spheroids having an axis ratio of 0.6. This axis ratio has been obtained from the in situ studies by Hogan et al. (2002). Above an ML, such an ice spheroid produces Z_{DR} in an interval of 1.5–2.5 dB depending on the intensity of flutter (Fig. S12, the corresponding σ_θ interval is 20°–5°). This Z_{DR} interval is a typical one in situations with no aggregation above MLs (e.g., Figs. S5 and S7). If a water film of $0.03a$ uniformly covers the ice core, the ρ_{hv} drops and δ increases (Fig. 10) compared to the values for the ice core (Fig. S12). The parameter $a = 1$ mm was used in the calculations. Polarizabilities α_a and α_b have been calculated using equations for layered scatterers (e.g., Bohren and Huffman 1983, section 5.4). Zero mean canting angle has been assumed in the calculations because of symmetry of the particle. For zero mean canting, the Z_{DR} values are not affected by ψ_i, but depend on σ_θ. The corresponding Z_{DR} values are shown in Fig. 10a with numbers. The Z_{DR} values are about equal to those observed in the melting layer (Figs. S5 and S7). One can see that the differential phase ψ_i strongly affects ρ_{hv} and δ values (Fig. 10). The maximal impact on δ is about 2.6° at $\psi_i = 90°$. For the ice particle without the water cover, the maximal δ is 0.5° (Fig. S12).

Water can cover a particle nonuniformly. Due to moderate fall velocities associated with small particles, the larger density of water compared to the ice core can cause the water to form a hanging drop at the bottom of the falling particle (Fig. S13). The scattering properties of such particles cannot be obtained analytically even in the Rayleigh limit; therefore, the WIPL-D software has been used. The ice core diameter was assumed to be 1 mm, and the bottom water droplet maximal width was assumed to be 0.15 mm (Fig. S13).

If a layer of low Z_{DR} exists above an ML (e.g., Figs. S6 and S9), particles falling into MLs can be represented as aggregates of ice columns (e.g., Fabry and Zawadzki 1995; Fabry and Szyrmer 1999). Water in such particles can occupy a part of the aggregate or can cover ice crystals completely. To examine this situation, a particle has been modeled as one having two parts: an inner part consisting of a mixture of ice and water and an outer part consisting of ice and air (Fig. S14). Both particle's parts are treated as the Maxwell Garnett mixtures with the inner part containing 80% of ice and 20% of water and the outer layer consisting of 10% of ice and 90% of air. Dielectric permittivities of the inner and outer parts have been calculated via the Maxwell Garnett equation (e.g., Bohren and Huffman 1983, section 8.5; Ishimaru 1991) and the whole particle has been treated as a shielded particle (Bohren and Huffman 1983, section 5.4). The axis ratio of the particle assumed to be 0.6 and equal for the inner part and whole particle. Let the major axis of the whole particle be 1.5 times the major axis of its inner part. The δ values from this particle are

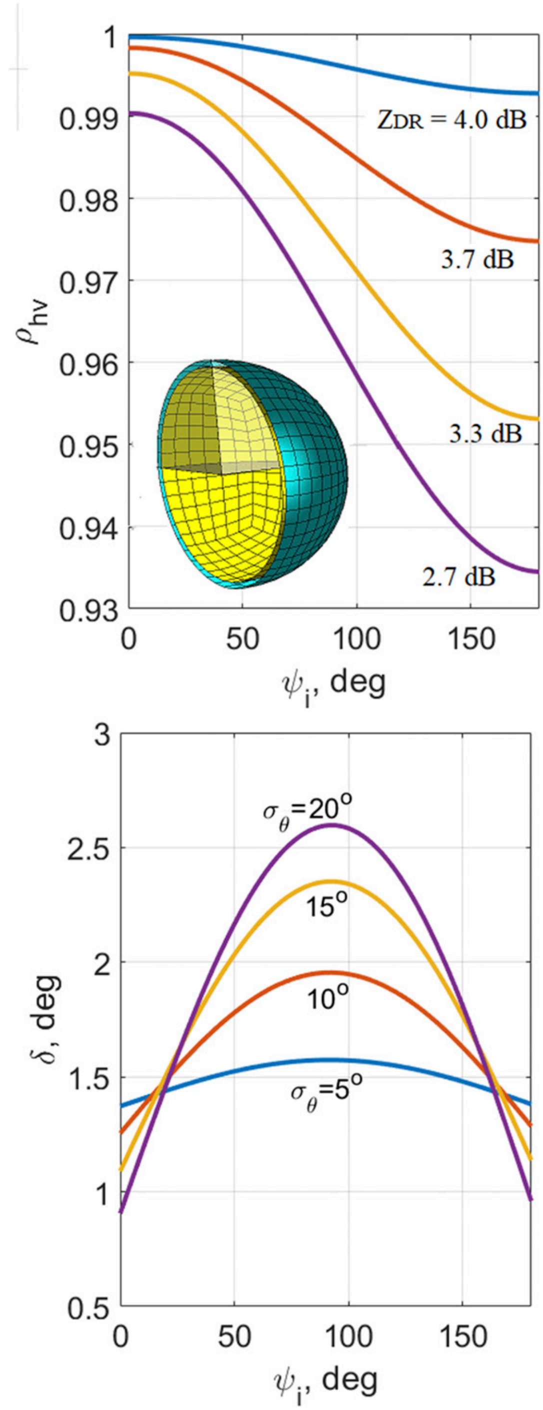

FIG. 10. Dependences of (top) ρ_{hv} and (bottom) δ on the incident differential phase and flutter intensity (σ_θ) for an ice spheroid uniformly covered with a water film. The axis ratio of the spheroid is 0.6 and the water cover thickness is 0.03 of its longest axis. The legends in the panels are applicable for all curves. The insert in the top panel shows half of the ice core (yellow) covered with a water film (blue).

significantly lower than those for the previous models (previous models are shown in Figs. 10 and 11; the current model is shown in Fig. 12). The radar variables from the model particles are close to those shown in the supplemental material (Fig. S6). The models show that the influence of ψ_i and σ_θ on radar variables is significant.

The presented results demonstrate that the radar variables from melting layers can be satisfactorily represented at S band by Rayleigh particles and the SHV δ values can emerge at scattering by incident waves shifted in phase. If adjacent radars feature different ψ_t, they can measure different polarimetric variables from same ice cloud areas.

The results in this section have been obtained for fluttering particles having a zero-mean canting angle. Asymmetrical ice particles have nonzero-mean canting angles. A wet ice particle can be asymmetrical if water is concentrated not at the center of a symmetrical ice part. Figure S15 shows a symmetrical ice dendrite with a small droplet at one of its branches. The particle acquires a nonzero equilibrium canting angle and its scattering characteristics can significantly deviate from those obtained for zero canting angle.

6. Conclusions

Weather radars employing simultaneous transmission and reception of orthogonally polarized waves (SHV design) deliver biased radar variables compared to those from alternate transmission radars (AHV design). In the SHV mode, the incident waves are typically shifted in phase (ψ_i) thereby affecting measured Z_{DR}, ρ_{hv}, and δ values due to interference between the scattered primary and depolarized waves. Maximal Z_{DR} values from thin ice plates measured with AHV radar is 10 dB, whereas for SHV radar it is 12.3 dB. Values of δ from thin ice cloud particles measured with AHV radar are of a few hundredths of a degree, whereas for SHV radar, maximal δ is 62.3° (section 2). For ice particles of moderate axis ratios, δ can reach 20° (for a width/length ratio = 0.3). Z_{DR} = 12.3 dB and δ = 62.3° are maximal possible values for Rayleigh ice particles other than thin plates. The maximal possible Z_{DR} value of 12.3 dB is much larger than measurement Z_{DR} limits on some radars. For example, the Z_{DR} span on WSR-88D is ±7.9 dB circa 2020 (WSR-88D Radar Operations Center 2018). Since 12.3 dB is the mean value and radar signals experience natural fluctuations, the maximal measurable Z_{DR} limit should be at least 15 dB for measurements in clouds.

The SHV δ values can be positive and negative depending on orientation of particles and the differential phase ψ_i. Typically, Z_{DR} and δ have the same sign that is intuitively clear. The analysis in section 2 shows that

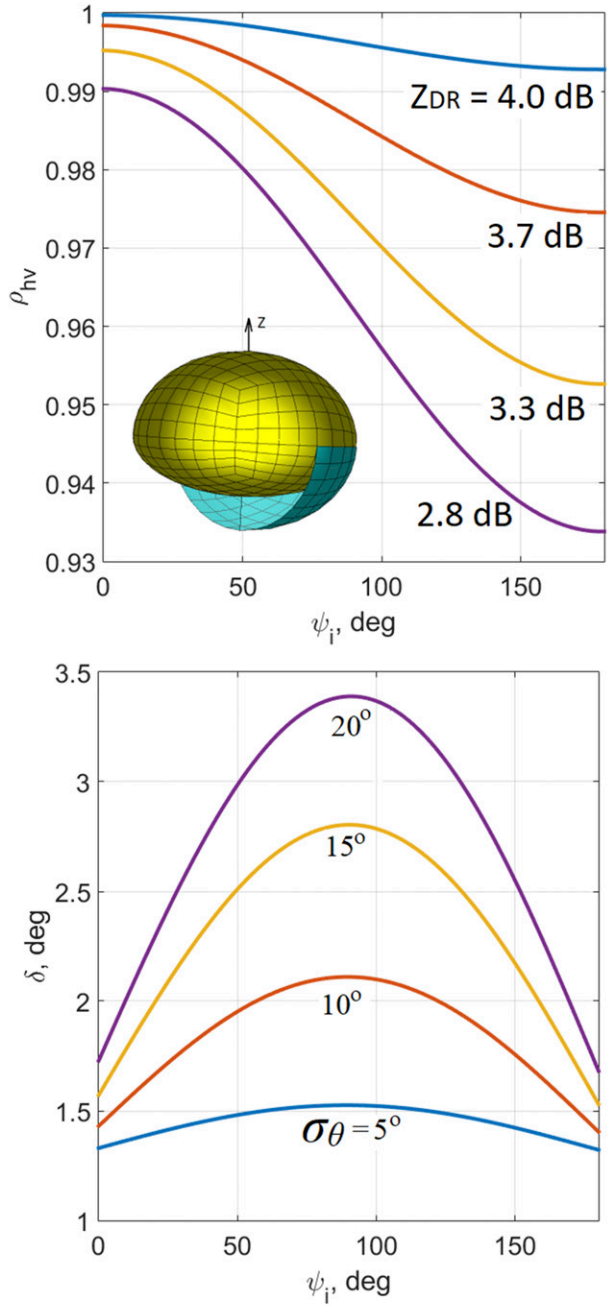

FIG. 11. As in Fig. 10, but for an ice spheroid (yellow in the insert) with a water drop (blue) at its bottom (Fig. S13). In the insert, half of the outer surface of water drop (blue) is shown for better viewing.

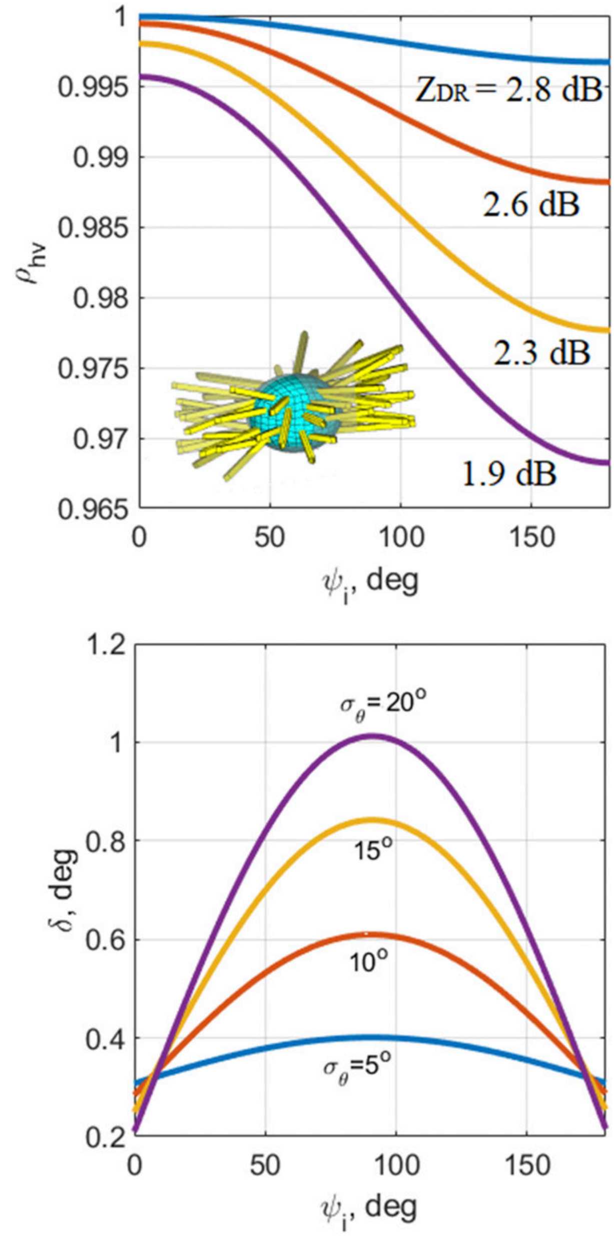

FIG. 12. As in Fig. 10, but for a particle sketched in Fig. S13 and in the insert. The ice aggregate is modeled as a collection of ice columns (yellow) and the water droplet is shown in blue.

particles producing positive Z_{DR} can exhibit negative δ and vice versa depending on their orientation relative to the radar beam and ψ_{i}.

The SHV δ values are of a few to several degrees depending on the axis ratio of a particle. Therefore, measured δ can be used in retrieval microphysical procedures if ψ_{t} is known (measured). Ice particles in shapes of ellipsoids and hexagonal prisms of the same axis ratios (width/length $= b/a$) produce different Z_{DR} and δ at $b/a > 0.1$ that should be taken into account in the retrieving of particles' parameters from radar data. The δ is a part of the measured total differential phase from which the specific differential phase (K_{DP}) is obtained. In precise K_{DP} measurements in snow and ice clouds, the contribution from δ should be accounted for.

Fluttering of ice particles significantly affects the polarimetric variables. Flutter of particles is an additional unknown parameter, which complicates the interpretation of radar data. The intensity of flutter is characterized with the standard deviation in the canting angles. The latter parameter depends not only on flutter, but also on the spread of canting angles due to asymmetry in particles' shapes.

The phase ψ_{i} contributes to the Z_{DR}, ρ_{hv}, and δ values observed in melting layers. Presented results show that such values of the radar variables can be produced by Rayleigh scatterers and there is no need to assume the presence of large particles of resonance sizes. The presented results show impacts of ψ_{i} on the δ and ρ_{hv} values in melting layers for some simple models of particles; the results correspond to data collected with S-band KOUN. Polarization properties of melting ice particles can be modeled using WIPL-D, a software tool allowing composition and analysis of ice and water together in a particle.

Dependences of Z_{DR}, ρ_{hv}, and δ values on the radar system differential phase upon transmission (ψ_{t}) point to additional measurement opportunities. Variations in ψ_{t} during the radar dwell time can deliver additional information about scatterers in real time. Fast ψ_{t} variations can be available on phased array radars, where alternations in ψ_{t} can be accomplished by changing a time delay between transmitted polarized waves.

Acknowledgments. The author thanks Dr. Terry Schuur for valuable comments and the reviewers for their suggestions, which helped to improve the presentation. Mr. Tomislav Milosevic from the WIPL-D company provided helpful advices on the WIPL-D modeling. Funding for this study was provided in part by the NOAA/Office of Oceanic and Atmospheric Research under NOAA–University of Oklahoma Cooperative Agreement NA110OAR4320072, U.S. Department of Commerce.

REFERENCES

ANSYS, 2020: 3D electromagnetic field simulator for RF and wireless design. ANSYS, Inc., accessed March 2020, https://www.ansys.com/products/electronics/ansys-hfss/.

Auer, A. H., and D. L. Veal, 1970: The dimension of ice crystals in natural clouds. *J. Atmos. Sci.*, **27**, 919–926, https://doi.org/10.1175/1520-0469(1970)027<0919:TDOICI>2.0.CO;2.

Bohren, C. F., and D. R. Huffman, 1983: *Absorption and Scattering of Light by Small Particles*. John Wiley and Sons, 530 pp.

Bringi, V. N., and V. Chandrasekar, 2001: *Polarimetric Doppler Weather Radar: Principles and Applications*. Cambridge University Press, 636 pp.

Caylor, I. J., and V. Chandrasekar, 1996: Time-varying crystal orientation in thunderstorms observed with multiparameter radar. *IEEE Trans. Geosci. Remote Sens.*, **34**, 847–858, https://doi.org/10.1109/36.508402.

Chobanyan, E., N. J. Šekeljić, A. B. Manić, M. M. Ilic, V. N. Bringi, and B. M. Notaros, 2015: Efficient and accurate computational electromagnetics approach to precipitation particle scattering analysis based on higher-order method of moments integral equation modeling. *J. Atmos. Oceanic Technol.*, **32**, 1745–1758, https://doi.org/10.1175/JTECH-D-15-0037.1.

Doviak, R. J., and D. S. Zrnić, 2006: *Doppler Radar and Weather Observations*. 2nd ed. Academic Press, 562 pp.

——, V. Bringi, A. Ryzhkov, A. Zahrai, and D. Zrnić, 2000: Considerations for polarimetric upgrades to operational WSR-88D radars. *J. Atmos. Oceanic Technol.*, **17**, 257–278, https://doi.org/10.1175/1520-0426(2000)017<0257:CFPUTO>2.0.CO;2.

Draine, B. T., and P. J. Flatau, 1994: Discrete-dipole approximation for scattering calculations. *J. Opt. Soc. Amer.*, **11A**, 1491–1499, https://doi.org/10.1364/JOSAA.11.001491.

Fabry, F., and I. Zawadzki, 1995: Long-term radar observations of the melting layer of precipitation and their interpretation. *J. Atmos. Sci.*, **52**, 838–851, https://doi.org/10.1175/1520-0469(1995)052<0838:LTROOT>2.0.CO;2.

——, and W. Szyrmer, 1999: Modeling of the melting layer. Part II: Electromagnetic. *J. Atmos. Sci.*, **56**, 3593–3600, https://doi.org/10.1175/1520-0469(1999)056<3593:MOTMLP>2.0.CO;2.

FEKO, 2020: FEKO. Accessed March 2020, http://www.antenna-theory.com/tutorial/feko/feko.php.

Garrett, T. J., S. E. Yuter, C. Fallgatter, K. Shkurko, S. R. Rhodes, and J. L. Endries, 2015: Orientation and aspect ratios of falling snow. *Geophys. Res. Lett.*, **42**, 4617–4622, https://doi.org/10.1002/2015GL064040.

Griffin, E., T. Schuur, and A. Ryzhkov, 2018: A polarimetric analysis of ice microphysical processes in snow, using quasi-vertical profiles. *J. Appl. Meteor. Climatol.*, **57**, 31–50, https://doi.org/10.1175/JAMC-D-17-0033.1.

——, ——, and ——, 2020: A polarimetric radar analysis of ice microphysical processes in melting layers of winter storms using S-band quasi-vertical profiles. *J. Appl. Meteor. Climatol.*, **59**, 751–767, https://doi.org/10.1175/JAMC-D-19-0128.1.

Hendry, A., and G. C. McCormick, 1976: Radar observations of alignment of precipitation particles by electrostatic fields in thunderstorms. *J. Geophys. Res.*, **81**, 5353–5357, https://doi.org/10.1029/JC081i030p05353.

Hogan, R. J., P. R. Field, A. J. Illingworth, A. J. Cotton, and T. W. Choularton, 2002: Properties of embedded convection in warm-frontal mixed-phase cloud from aircraft and polarimetric radar. *Quart. J. Roy. Meteor. Soc.*, **128**, 451–476, https://doi.org/10.1256/003590002321042054.

——, L. Tian, P. R. A. Brown, C. D. Westbrook, A. J. Heymsfield, and J. D. Eastment, 2012: Radar scattering from ice aggregates using the horizontally aligned oblate spheroid approximation. *J. Appl. Meteor. Climatol.*, **51**, 655–671, https://doi.org/10.1175/JAMC-D-11-074.1.

Holt, A. R., 1984: Some factors affecting the remote sensing of rain by polarization diversity radar in 3- to 35-GHz frequency range. *Radio Sci.*, **19**, 1399–1412, https://doi.org/10.1029/RS019i005p01399.

Hubbert, J. C., S. M. Ellis, W.-Y. Chang, S. Rutledge, and M. Dixon, 2014a: Modeling and interpretation of S-band ice crystal depolarization signatures from data obtained by simultaneously transmitting horizontally and vertically polarized fields. *J. Appl. Meteor. Climatol.*, **53**, 1659–1677, https://doi.org/10.1175/JAMC-D-13-0158.1.

——, ——, ——, and Y.-C. Liou, 2014b: X-band polarimetric observations of cross coupling in the ice phase of convective storms in Taiwan. *J. Appl. Meteor. Climatol.*, **53**, 1678–1695, https://doi.org/10.1175/JAMC-D-13-0360.1.

——, J. M. Wilson, T. Weckwerth, S. M. Ellis, M. Dixon, and E. Loew, 2018: S-POL's polarimetric data reveal detailed storm features (and insect behavior). *Bull. Amer. Meteor. Soc.*, **99**, 2045–2060, https://doi.org/10.1175/BAMS-D-17-0317.1.

Ishimaru, A., 1991: *Electromagnetic Wave Propagation, Radiation, and Scattering*. Prentice Hall, 637 pp.

Matrosov, S. Y., 2015: Evaluations of the spheroidal particle model for describing cloud radar depolarization ratios of ice hydrometeors. *J. Atmos. Oceanic Technol.*, **32**, 865–879, https://doi.org/10.1175/JTECH-D-14-00115.1.

Melnikov, V., 2017: Parameters of cloud ice particles retrieved from radar data. *J. Atmos. Oceanic Technol.*, **34**, 717–728, https://doi.org/10.1175/JTECH-D-16-0123.1.

——, and J. M. Straka, 2013: Axis ratios and flutter angles of cloud ice particles: Retrievals from radar data. *J. Atmos. Oceanic Technol.*, **30**, 1691–1703, https://doi.org/10.1175/JTECH-D-12-00212.1.

——, D. Zrnić, R. Rabin, and P. Zhang, 2008: Radar polarimetric signatures of fire plumes in Oklahoma. *Geophys. Res. Lett.*, **35**, L14815, https://doi.org/10.1029/2008GL034311.

——, ——, and ——, 2009: Polarimetric radar properties of smoke plumes: A model. *J. Geophys. Res.*, **114**, D21204, https://doi.org/10.1029/2009JD012647.

Mishchenko, M. I., L. D. Travis, and A. A. Lacis, 2002: *Scattering, Absorption, and Emission of Light by Small Particles*. Cambridge University Press, 453 pp.

Pruppacher, H. R., and J. D. Klett, 1997: *Microphysics of Clouds and Precipitation*. Kluwer Academic, 954 pp.

Purcell, E. M., and C. R. Pennypacker, 1973: Scattering and absorption of light by nonspherical dielectric grains. *Astrophys. J.*, **186**, 705–714, https://doi.org/10.1086/152538.

Ryzhkov, A. V., and D. S. Zrnić, 2007: Depolarization in ice crystals and its effect on radar polarimetric measurements. *J. Atmos. Oceanic Technol.*, **24**, 1256–1267, https://doi.org/10.1175/JTECH2034.1.

Trömel, S., M. R. Kumjian, A. V. Ryzhkov, C. Simmer, and M. Diederich, 2013: Backscatter differential phase—Estimation and variability. *J. Appl. Meteor. Climatol.*, **52**, 2529–2548, https://doi.org/10.1175/JAMC-D-13-0124.1.

——, A. V. Ryzhkov, P. Zhang, and C. Simmer, 2014: Investigations of backscatter differential phase in the melting layer. *J. Appl. Meteor. Climatol.*, **53**, 2344–2359, https://doi.org/10.1175/JAMC-D-14-0050.1.

Vivekanandan, J., W. M. Adams, and V. N. Bringi, 1991: Rigorous approach to polarimetric radar modeling of hydrometeor orientation distributions. *J. Appl. Meteor.*, **30**, 1053–1063, https://doi.org/10.1175/1520-0450(1991)030<1053:RATPRM>2.0.CO;2.

——, V. N. Bringi, M. Hagen, and P. Meischner, 1994: Polarimetric radar studies of atmospheric ice particles. *IEEE Trans. Geosci. Remote Sens.*, **32**, 1–10, https://doi.org/10.1109/36.285183.

Wang, Y., V. Chandrasekar, and V. N. Bringi, 2006: Characterization and evaluation of hybrid polarization observation of precipitation. *J. Atmos. Oceanic Technol.*, **23**, 552–572, https://doi.org/10.1175/JTECH1869.1.

Westbrook, C. D., 2014: Rayleigh scattering by hexagonal ice crystals and the interpretation of dual-polarization radar measurements. *Quart. J. Roy. Meteor. Soc.*, **140**, 2090–2096, https://doi.org/10.1002/qj.2262.

WIPL-D, 2020: WIPL-D. Accessed March 2020, https://wipl-d.com.

Wolde, M., and G. Vali, 2001: Polarimetric signatures from ice crystals observed at 95 GHz in winter clouds. Part I: Dependence on crystal form. *J. Atmos. Sci.*, **58**, 828–841, https://doi.org/10.1175/1520-0469(2001)058<0828:PSFICO>2.0.CO;2.

WSR-88D Radar Operations Center, 2018: Interface control document for the RDA/RPG. WSR-88D Radar Operations Center Doc. 2620002R, 135 pp., https://www.roc.noaa.gov/wsr88d/PublicDocs/ICDs/2620002R.pdf.